Cryptomelane nanocrystals: Pseudosymmetry causes anisotropic peak broadening in Rietveld refinement

Cryptomelane nanocrystals: pseudosymmetry causes anisotropic peak broadening in Rietveld refinement

Alice Boschetti*[1] and Miguel Gregorkiewitz*

Department of Physical, Earth and Environmental Sciences, University of Siena, via Laterina 8, I-53100 Siena, Italy.

[1] Present address: European Laboratory for Non-Linear Spectroscopy (LENS), University of Florence, via Nello Carrara 1, I-50019 Sesto Fiorentino, Italy.

E-mail: alibosche@gmail.com, gregormigu@gmail.com.

ORCID

Alice Boschetti https://orcid.org/0000-0001-5531-6924

Miguel Gregorkiewitz https://orcid.org/0000-0001-8566-4401

Published Article: https://doi.org/10.1016/j.jssc.2023.124212

Abstract

Cryptomelane ($\square_{2-x}K_x$)[Mn_8O_{16}] is an octahedral molecular sieve with the hollandite framework, a strongly correlated electron system with tunnel structure. Rietveld refinement using powder X-ray diffraction patterns of a nanocrystalline sample was undertaken to assess both structural and morphological details which might be tuned for specific applications. The distribution of peak widths was highly anisotropic but successful refinement of the tetragonal structure could be achieved assuming both grain shape and microstrain anisotropy. The microstrain hypothesis appeared flawed from high uncertainties and correlations and was in conflict with the negative slope of a Williamson-Hall plot. As an alternative, lattice desymmetrization from tetragonal to monoclinic was considered. Comparison of calculated and observed *hkl* dependence of line broadening confirmed that the pseudosymmetry hypothesis was more appropriate, improving results for both structure and particle shape. This is the first time that lattice desymmetrization was used to explain anisotropic diffraction line broadening, a major issue in nanomaterials where peaks are intrinsically broad and the new model helps to abate correlations.

KEYWORDS

potassium hollandite, metal oxide semiconductors, grain size, grain shape, microstrain, desymmetrization

1. Introduction

Cryptomelane and its derivatives ($\square_{2-x}A_x$)[Mn_8O_{16}], A=Li,Na,K,Rb,Cs,Ag), like other octahedral molecular sieve structures with large tunnels, are intensively studied for many applications. They are widely recognized redox catalysts substituting and outperforming noble metals, e.g. for the total oxidation of formaldehyde [1-3] and benzene [4,5] (two important carcinogens) or for selective oxidation reactions like alcohol to ketone [6-9]; they have been proposed for CO_2 capture [10] and might also be able to intercalate N_2 [11]; they have been studied for chemical sensors [12-14] and multiferrroics [15]; and they are now at the centre of attention for electrodes in batteries [16-21], as well as for Faradaic electrodes in supercapacitors either in high power electrochemical cells [22-24] or in capacitive water deionization [25,26] and its reverse, the harnessing of energy from a salinity gradient [27].

For most of these applications, the particle size is of fundamental importance and nanoparticles are preferred. In heterogeneous catalysis, reactions take place at the surface of a solid [7,8]; in gas chemical sensors the target gas is adsorbed at the grain surface and causes the build up of electrostatic potentials which modify the electric conductivity used to get the concentration and identity of the gas [28-30]; and in electrodes, where the crystal structure determines the ion-exchange capacity, short diffusion lengths from the surface to the bulk are required to improve reaction rates [23,24,26].

The development of new materials must therefore consider both particle size and crystal structure. The crystal structure defines the geometry of the facet at the surface which is thought to be fundamental for the interaction with molecules [3, 31] but there are also details regarding composition [4, 21, 32, 33], symmetry [21, 33, 34], electronic structure [31, 32] and intracrystalline diffusion [33] which may be of crucial importance in many of the above cited applications.

Here, we present the Rietveld refinement of a synthetic nanocrystalline cryptomelane, a

potassium hollandite structure that has the unit cell composition $(\square_{2-x}K_x)[Mn^{3+}{}_xMn^{4+}{}_{8-x}O_{16}]$ and that is based on an open framework of MnO_6 octahedra (in brackets) where variable quantities of potassium ($0 \leq x \leq 2$ per unit cell) are accommodated in a tunnel running along the crystallographic **c** axis (Fig. 1). The positive charge of potassium is compensated by a $Mn^{4+} \rightarrow Mn^{3+}$ substitution in the framework which changes the electron configuration of manganese from $3d^3$ to $3d^4$, with possible consequences on electronic structure and band gap of the semiconductor. On the other hand Mn^{3+}, in its high-spin configuration, is known [35] to be subject to a strong Jahn-Teller effect which might be recognized from a distortion of the Mn-O octahedral bond distances. It was therefore important to conduct the Rietveld refinement appropriately in order to get exact information about the degree of substitution *x* and possible octahedral bond length distortions along with a correct description of the particle size.

The Rietveld method has initially been developed for the refinement of crystal structures where single crystals were not available. In this context, width and shape of the peaks had to be well simulated in order to optimize the extraction of intensities, but their physical meaning was of subordinate interest. During the 90's, profile models were improved (e.g. [36-38]) and it became eventually routine [39,40] to use profile parameters for getting information about the microstructure of a sample. In nanomaterials, grain[1] size is the dominant cause for line broadening, which may vary with the direction of the diffraction vector if the shape deviates from spherical, but microstrain is another source of (generally anisotropic) line broadening which is frequently observed. It is a well known problem [39] that, in many cases, grain size and microstrain parameters tend to correlate in Rietveld refinements, and special care regarding the number and choice of refined parameters is needed to obtain meaningful results.

In our refinement, we started keeping the number of profile parameters as low as possible,

1 We use “grain”, shortly, for the coherently diffracting domain or “crystallite”

but soon it became clear that grain size anisotropy alone was not sufficient to correctly describe the observed anisotropic line broadening, and additional peak shape models had to be introduced. The strong *hkl* dependence of peak widths was tentatively simulated in two alternative approaches, first taking a microstrain model [38], and then developing a new model where peak splitting due to a slight desymmetrisation of the originally tetragonal unit cell ($b = a+\delta a$, $\gamma = 90^{o}+\delta\gamma$) contributes to line broadening. The second model turned out to be more appropriate for the present material.

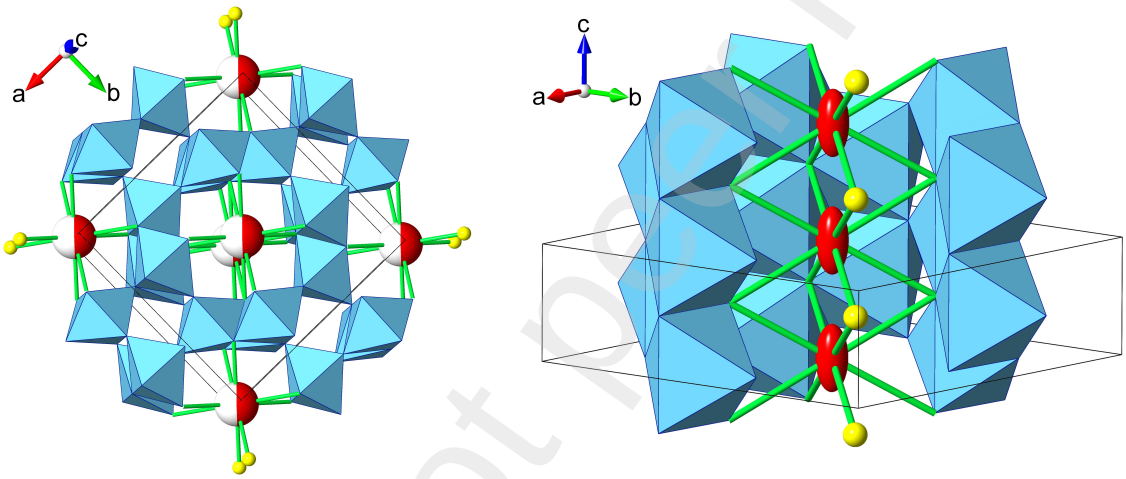

Fig. 1. Crystal structure of cryptomelane ($\square_{2-x}K_x$)[Mn_8O_{16}] in quasi-projection (left) and zoomed perspective view (right) showing the octahedral 2×2 framework [41] of hollandite and the coordination of potassium in the tunnels running along **c** (space group *I*4/*m*, a = 9.840 Å, c = 2.8516 Å; MnO_6 octahedra light blue, K sites red with filled sector indicating the degree of occupation, oxygen yellow or octahedral apex). There are two tunnels per unit cell (outlined box), each of them containing one K site in a square prism with d(K-O) = 2.90 Å. Graphics prepared using VESTA [42].

2. Materials and methods

2.1. Synthesis

The cryptomelane sample used for this study was prepared in a teflon lined steel autoclave at 100ºC following the procedure of DeGuzman et al. [43], except for the addition of K_2SO_4 as will be explained in the results section. Reagents were $KMnO_4$ (Merck, p.a.), $MnSO_4 \cdot H_2O$ (Merck, p.a.), 70% HNO_3 (Panreac, ACS) and K_2SO_4 (BDH, AnalaR). The chemical composition was obtained from EDX spectra in a Philips XL30 scanning electron microscope at 20 kV acceleration tension and a take off angle of 35º, accumulation time 50 s at about 2500 cps, and applying the ZAF correction. Values and their standard deviations were obtained from averaging over the results for five different homogeneous areas of about 10×10 μm^2.

2.2. Powder X-ray diffraction

X-ray diffraction patterns were obtained using an automated Philips PW1050/PW1710 powder diffractometer with Bragg-Brentano geometry, CuKα radiation (λ = 1.540598 and 1.544418 Å), a graphite (002) secondary beam monochromator and a proportional counter allowing for pulse height discrimination ($\Delta V/V$~0.2). Axial divergence was defined by 2*0.04 rad Soller slits in the incident and the diffracted beam, divergence in the diffraction plane was 1º, and the resolution slit on the Seemann-Bohlin parafocusing circle was 0.2 mm. The powder was placed in a Si(100) single crystalline sample holder (28*18*1.38 mm^3) in order to minimize background, and data were collected in θ-2θ scans from 5º to 120º(2θ) at 0.02º(2θ) step intervals and 4 s per step. Intensities were corrected for the LP factor and, below 12.58º(2θ), also for beam overspill.

2.3. Interpretation of diffraction patterns

The GSAS program system [44] combined with the EXPGUI graphical interface [45] were used for Rietveld refinement least squares calculations. The background was simulated using

a 15-term (18 in the final stage of refinement) Chebyshev function, and peak profiles were calculated using a TCH pseudo-Voigt function [46] providing for up to six refined parameters as specified in the results section. Five instrument dependent profile parameters (the Gaussian variances *U*, *V* and *W* of Caglioti et al. [47] and the asymmetry terms *H*/*L* and *S*/*L* of Finger et al. [37]) were found from independent refinements using standard materials (3 μm silicon powder and synthetic zeolite MFI, respectively) and hold constant throughout all calculations.

For two peaks (110 and 200, Supplementary Material S2), fitting to a TCH doublet was achieved using a home-made scilab [48] code.

3. Results and discussion

3.1. Synthesis

The synthesis of cryptomelane $(\square_{2-x}K_x)[Mn^{3+}{}_xMn^{4+}{}_{8-x}O_{16}]$ corresponds to a redox comproportionation

$$(2-z)/5\ KMn^{7+}O_4 + (3+z)/5\ Mn^{2+}SO_4{\cdot}H_2O \rightarrow$$

$$\rightarrow\ K_z[Mn^{(4-z)+}O_2] + (1-3z)/5\ H_2O + 4(1+2z)/5\ H^+ + 2(1-3z)/5\ K^+ + (3+z)/5\ SO_4^{2-} \qquad (1)$$

where the degree of substitution $x=8z$ should be given by the stoichiometry of the reactants as defined in equation (1), but in practice, a cryptomelane with $x\sim1$ is obtained over a wide range of batch compositions which lie between $q = [Mn^{7+}]/([Mn^{7+}]+[Mn^{2+}]) = 0.36$ and 0.88 [43], indicating that conditions may be much more oxidizing than expected for a negatively charged framework (q=0.350, 0.375 and 0.400 for x=2, 1 and 0, respectively). The presence of potassium might be important for nucleation, and we therefore modified the batch composition of DeGuzman et al. [43] increasing the concentration of K by the addition of a

redox-inert salt (K_2SO_4) while keeping the original value q=0.42. The actual batch composition was (in mmol) 3.7 $KMnO_4$ + 5.2 $MnSO_4 \cdot H_2O$ + 4.9 HNO_3 + 3.7 K_2SO_4 in 13 mL H_2O.

After reaction, the dark brown slurry was washed and filtered until the effluent gave neutral pH, and the solid was dried at 90ºC for 24h. Energy dispersive X-ray (EDX) spectroscopy results for the chemical composition were normalized to 8 Mn per formula and gave the mean values (uncertainties on last digit in parentheses) 0.93(3) K, 18(2) O and 0.08(1) S. The uncertainty for oxygen is high, indicating that there is no significant deviation from the expected value (16 O), and sulphur is thought to be present as traces of the SO_4^{2-} introduced during the synthesis. The potassium content of 0.93 indicates about half filling of the available sites in the channels.

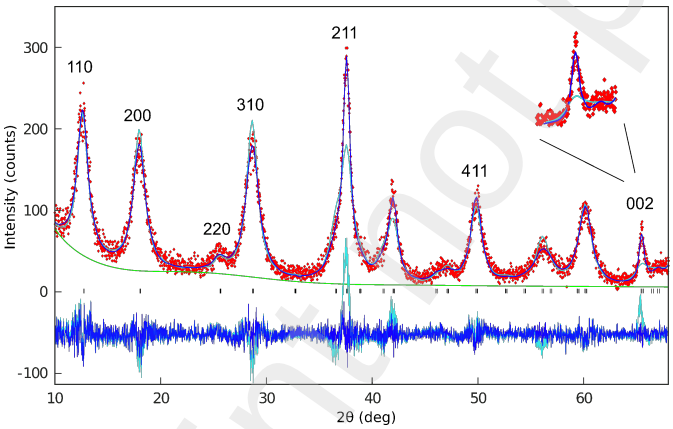

Fig. 2. Observed (dots), calculated (line) and difference (below) intensities for the powder diffraction pattern of synthetic cryptomelane ($\square_{2-x}K_x$)[Mn_8O_{16}]. Blue corresponds to the final model (χ^2 = 1.18), cyan to the first model (isotropic grains, χ^2 = 1.60). Green (smooth) line is background. Ticks show possible positions for reflections in the tetragonal unit cell, indices *hkl* are given for seven non overlapping peaks (the weak satellites near 211 can be neglected for the present purpose). λ(CuKα) = 1.540598 and 1.544418 Å.

3.2. Rietveld refinement

Rietveld refinement started from the unit cell and atom parameters of Vicat et al. [49] but setting potassium to its ideal position at the centre of the cavity ($z = 0.5$). Scattering factors for fully ionized species were used for all atoms. In a first step, only the site occupation factor (*SOF*) of potassium, isotropic atom displacement parameters (restrained to be equal for the two oxygen positions), cell parameters, background, 2θ origin and a Lorentzian describing isotropic line broadening (for both grain size and microstrain) were allowed to refine, converging to a model with the error indices $\chi^2 = 1.60$, $R_p = 0.140$, $R(F^2) = 0.0855$.

This model was not able to reproduce the observed peak widths which are generally broad but change from one line to the other (Fig. 2) and show a striking minimum for 002, indicating that the coherent domains are considerably more extended along **c**, which is the direction of the octahedral chains. Introducing the corresponding grain size anisotropy[2], the model was considerably improved ($\chi^2 = 1.26$, $R_p = 0.122$, $R(F^2) = 0.0720$) and the 002 reflection was correctly simulated, but the variations of the broader peak widths were still not accounted for. Grain size anisotropy only provides for direction dependent peak widths, so we included also a microstrain model [38] which allowed for an *hkl* dependent variation and gave a further improvement ($\chi^2 = 1.186$, $R_p = 0.117$, $R(F^2) = 0.0622$).

The observed peak shape anisotropy was now fairly well simulated and it became possible to refine details of the crystal structure freeing *xy* for the Mn and O atoms and allowing K to move around its special position at $z = 0.5$, using either an anisotropic displacement tensor U_{ij} or a split position near $z = 0.4$. The two alternatives gave identical agreements ($\chi^2 = 1.184$, $R_p = 0.116$, $R(F^2) = 0.0627$) and indicate both that K is distributed along the **c**-axis over an interval of about 0.5 Å around its special position. Atom parameters and interatomic distances

2 A rotational ellipsoid (2 parameters) was used. Trials using spherical harmonics with up to 11 parameters were made with the help of program MAUD [50] but indicated no improvement.

and angles for the first alternative (Tables S1 and S2) are discussed in the Supplementary Material S1.

3.3. Crystal structure

The potassium site occupation factor of *SOF* = 0.493(15), in particular, translates into a degree of substitution of $x = 0.99(3)$, within the limits of error of the value $x = 0.93(3)$ found from chemical analysis. However, a higher *SOF* might also be caused by the presence of some water H_2O or hydronium H_3O^+ occupying empty K sites in the tunnel where it would be easily recognized from its effect on the diffracted intensities while detection by chemical analysis would be difficult. We therefore prefer to hold the analytical value of $x = 0.93(3)$ for the potassium site occupation, leaving the question of water/hydronium and its concomitant influence on the exact number of Mn^{3+} open for a future study.

Earlier work [49,51-53] about the hollandite structure has reported evidence for a displacement of tunnel cations from the special position and models considering repulsive forces between neighbouring sites have been put forward. In all of this work the degree of substitution x was significantly greater than 1, in contrast to our material where $x<1$ and potassium can easily be accommodated in alternating cavities, leaving the remainder free or occupied by water, without any repulsive interactions producing displacement. The alternative with the special position was therefore chosen for the final parameters (Table S1).

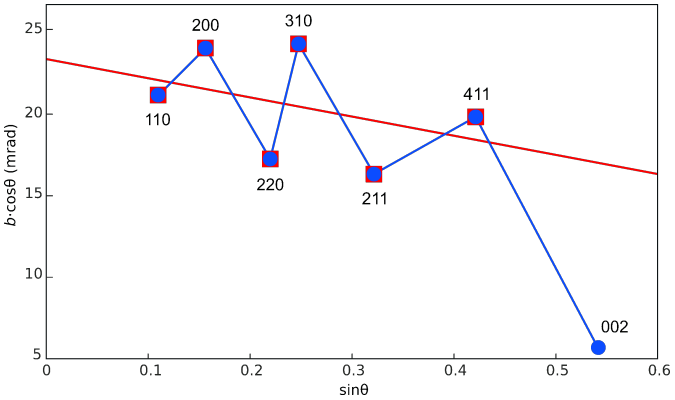

Fig. 3. Williamson-Hall plot of the observed line widths $b = B - b_i$ (milliradians) for non overlapping reflections of synthetic cryptomelane. Line widths B were obtained from fitting each peak individually using eight parameters (one position, two widths, three intensities and a linear background) allowing for three (fixed) wavelengths (α0, α1, and α2) where α1 and α2 have their usual meaning and α0 is a broad dummy of low intensity to abate peak asymmetry at low angles. Line widths, obtained in terms of *FWHM*, are therefore free from contributions due to α1-α2 splitting and asymmetry. The instrument contribution b_i to line width is small (see text). The regression line refers to the first six points.

3.4. Microstrain vs desymmetrization

The results of Rietveld refinement also contain six parameters extracted from peak shape anisotropy. In principle, grain size and microstrain are described by a different set of profile parameters, but in practice they may correlate if peaks are broad and strongly overlapped as it necessarily happens with nanocrystals. In our case, the four microstrain parameters, in particular, showed uncertainties of 23-75% (*cf* 3-8% for the grain size parameters) and correlations of up to 0.91 which shed doubt on their physical meaning.

In order to get an independent and robust test about the presence of microstrain, a Williamson-Hall plot [54,55] was drawn using seven selected, non-overlapping reflections (Fig. 3). The peak widths b, corrected for the instrumental broadening ($b_i/^o = 0.0761 + 0.0465 \tan\theta$) and multiplied with $\cos\theta$, should lie on a line complying with $b\cos\theta = K\lambda/D_V +$

$(4\delta d/d)\cdot\sin\theta$ where the intercept is related with the apparent grain size D_V and the slope with a microstrain term $|\delta d/d|$ giving the relative deformation around the mean of the spacing d_{hkl}. Note that $|\delta d/d|$ is a modulus without sign, so the negative slope of the regression line through the six broader peaks in Fig. 3 can hardly be explained by microstrain but is more likely due to grain size anisotropy: with the long axis parallel to 002, the 211 and 411 vectors are inclined with respect to the **ab** plane, making the corresponding grain dimensions longer than the short axis of a prolate rotational ellipsoid or cylinder which, in turn, is seen in the four *hk*0 reflections.

We therefore searched for alternative causes which might explain the *hkl* dependent variation of peak widths. A careful inspection of the diffraction pattern shows that some of the broader peaks with simple *hkl* indices (e.g. 110 and 200 in Fig. 2) suggest a splitting caused by desymmetrization of the structure from tetragonal to monoclinic symmetry so that the *hkl*, *khl*, $\bar{h}kl$ and $\bar{k}hl$ peaks would no longer coincide, in agreement with single crystal results [51] where monoclinic symmetry was found for cryptomelane. Taking the unit cell of Post et al. [51] an expected amount of splitting can be found from equations (3) and (4) which are derived from the formula for *d*-spacing of a monoclinic cell (2) considering but minor deviations from tetragonal ($b=a+\delta a$, $\gamma=90^\circ+\delta\gamma$); the splitting between *hkl* and $\bar{k}hl$ is the sum of (3) and (4).

$$(2\sin\theta/\lambda)^2 \equiv 1/d^2(hkl) = [h^2/a^2 + k^2/b^2 - 2hk\cos\gamma/ab] / \sin^2\gamma + l^2/c^2 \quad (2)$$

$$1/d^2(hkl) - 1/d^2(khl) = (h^2-k^2)\,[1-(1+\delta a/a)^{-2}]\,/a^2\sin^2\gamma \approx 2\,(h^2-k^2)\,(\delta a/a)\,/\,a^2 \quad (3)$$

$$1/d^2(hkl) - 1/d^2(\bar{h}kl) = 4\,hk\,[\sin\delta\gamma/(1+\delta a/a)]\,/a^2\sin^2\gamma \approx 4\,hk\,\sin\delta\gamma\,/\,a^2 \quad (4)$$

The corresponding values for $\Delta(2\theta)$ are reported in Table 1 and approximately reproduce the oscillations of the observed peak widths *b*. These results can immediately be exploited to

get an unbiased estimate of the grain dimensions. Excluding microstrain, we get the long axis directly from the peak width ($b_g = b$ = 6.9 mrad) of the non-split 002 reflection, and the short axis can be estimated from the width of the first reflections (110 and 200) which are doublets where the grain size contribution is $b_g = b - f\Delta(2\theta)$ with $f \leq 1$. Taking the values of b and $\Delta(2\theta)$ in Table 1 and $f = 1$, one obtains b_g = 17.7(16.3) mrad for 110(200) or an average of ~17.0 mrad assuming cylindrical particles (the correction for cosθ is almost nil). Similar values of b_g were obtained from tentative fittings of the 110 and 200 peaks to a doublet, which suggest that f might be a little smaller than unity (see Supplementary Material S2). For φ = 0 and 90º, the apparent domain sizes D_V are now directly calculated from the Scherrer relation $D_V = \lambda/(\beta_g \cos\theta)$, after conversion to integral breadths β using $\beta_g = (b_g\pi/2)/[\eta+(1-\eta)\sqrt{(\pi \ln 2)}]$ where a Lorentzian character η = 0.9 has been assumed.

Table 1. Observed and calculated peak width variations.

hkl	θ/º	*B*/º	*b*	φ/º	$\Delta(2\theta)$	γ_S	γ'_S
110	6.32	1.30	21.3	90	3.6	0.7	1.9
200	8.99	1.48	24.4	"	8.1	3.3	4.8
220	12.69	1.10	17.7	"	7.4	1.5	3.9
310	14.33	1.53	25.2	"	15.4	4.4	6.7
211	18.75	1.08	17.2	32.9	5.7	6.2	2.3
411	24.91	1.35	21.9	50.1	16.4	10.1	7.6
002	32.72	0.50	6.9	0	0	3.8	0

Symbols: *B* is the observed width *FWHM*, *b* (mrad) is the same corrected for instrumental broadening, φ is the angle between **c** and the vector *hkl*, $\Delta(2\theta)$ (mrad) is the difference in peak position due to desymmetrization ($\delta a/a$=0.02543, $\delta\gamma$=0.95), γ_S (mrad) is the contribution to *FWHM* calculated from the (four) microstrain parameters obtained in Rietveld refinement, and γ'_S (mrad) the same obtained from refinement with two microstrain parameters only (see text).

The resulting grain dimensions are 61*61*178 $Å^3$ which corresponds, assuming a cylinder, to a quite high specific surface area of 175 m^2/g, comparable to high end BET results for cryptomelane nanomaterials [56-59]. This estimate is most important for materials properties in sensor and catalytic applications.

From Fig. 3 one observes a pronounced oscillation of the line width *b* which follows the oscillation of $\Delta(2\theta)$ in Table 1, but it also reflects the strongly anisotropic grain shape which causes reflections with $\varphi \rightarrow 0$ to be sharper as discussed above. In our Rietveld refinement, the combined effect of *hkl* and direction dependent oscillation is simulated by microstrain broadening γ_s and grain shape. Values for γ_s are reported in Table 1 along with $\Delta(2\theta)$.

A comparison shows that both values and fluctuations of *b* are surprisingly well predicted by $\Delta(2\theta)$, whereas γ_s (note that these values are optimized by refinement) reproduces some of the fluctuations but is far from the correct values for the first and last (less model biased) reflections 110 and 002, and 310 turns out sharper than 211 instead of being broader as clearly observed in *b*. Both $\Delta(2\theta)$ and γ_s scale with *hkl*, but the pseudosymmetry model also contains differences $h^2–k^2$ which are absent in the microstrain model. As a consequence, and as expected from theory (see discussion of Fig. 3 above), γ_s increases more steadily (note the value for reflection 211) and requires a more pronounced grain size anisotropy to re-establish the negative observed slope in the Williamson-Hall plot (Fig. 3). This is indeed what happened during refinement which resulted in a (proforma) grain size of 48*48*232 $Å^3$.[3] Remembering the high correlations, the microstrain model (4 refined parameters) is therefore suspect to be an artefact of refinement, and the pseudosymmetry model (2 parameters, not refined in this study) seems more realistic.

3 Note that this differs by -21/+30% from the improved results mentioned above (61*61*178 $Å^3$), more than the variations which are sometimes discussed for different definitions of β, e.g. [60].

Tentatively, we tried a Rietveld refinement where the atom parameters were constrained to keep tetragonal symmetry but the unit cell was allowed to be monoclinic (see Supplementary Material S3). In this refinement, the four microstrain parameters were virtually substituted by the two desymmetrization parameters $\delta a/a$ and $\delta\gamma$ to simulate anisotropic line broadening. Very similar error indices were obtained, but without the excessive uncertainties and correlations which characterized the refinement containing microstrain.

Recently it has been argued [61] that microstrain and reflection splitting should be comparable in their contributions to (anisotropic) line broadening. In Stephens' model [38], the contribution of microstrain to *FWHM* is given by $\Gamma_s d^2 \tan\theta$ where, for powders of tetragonal symmetry,

$$\Gamma_s^2 = \Sigma_{HKL}(S_{HKL} h^H k^K l^L) = S_{400}(h^4+k^4) + S_{004} l^4 + 3S_{220} h^2 k^2 + 3S_{202}(h^2+k^2) l^2 \quad (5)$$

with H+K+L=4 and S_{HKL} (in $deg^2Å^{-4}$) the microstrain parameters to be refined. Reflection splitting due to desymmetrization from tetragonal to monoclinic $I112/m$ is invariant to index l, so that $S_{004}=S_{202}=0$ should hold, in our case, if anisotropic line broadening is due to desymmetrization. Leaving only two microstrain parameters to be refined, we obtained again lower uncertainties and correlations (see Supplementary Material S4) and, most importantly, the resulting contribution to *FWHM*, reported as γ_s' in the last column of Table 1, effectively shows a close resemblance to the trends observed for reflection splitting $\Delta(2\theta)$.

4. Conclusions

Desymmetrization as an explanation for peak shape anisotropy has only marginally been considered so far (a treatment of microstrain by Rodriguez-Carvajal et al. [62] and Rodriguez-

Carvajal [63] is formally comparable with equation (3), and a small orthorhombic deviation from tetragonal has been discussed by Fabrykiewicz et al. [64] in similar terms). It is therefore interesting, particularly in the context of nanocrystalline ceramics where peaks are intrinsically broad, to develop this model further and eventually include it in a Rietveld refinement code.

It seems interesting to note that desymmetrization acts more critically on peak positions than on diffracted intensities. The structure factor is a smooth function of atom positions which undergoes only minor changes in a structural desymmetrization. The matching of observed and calculated peak positions, on the other hand, is more akin to work with delta functions which change drastically upon minimal displacements. Lattice desymmetrization might therefore be an important improvement for correct peak profile descriptions also in high-resolution powder patterns.

The improved simulation of the diffraction pattern of a cryptomelane nanomaterial strongly suggests that the true symmetry of these materials is not tetragonal as assumed by most authors (e.g. [13,33,65,66]) but monoclinic (in agreement with results for larger particles [10,51]) which, most importantly, allows to obtain more reliable values for the nanoparticle size. The estimated surface area is relatively high and might be a consequence of potassium addition during synthesis.

Acknowledgements

We thank R. Cini and G. Tamasi at Dept Biotechnologies, Chemistry and Pharmacy, University of Siena, for their assistance in the synthesis, and S. Meroni, Swansea University, who did pioneering work in the early stage of synthesis. A. Zappettini at Istituto dei Materiali per l'Elettronica ed il Magnetismo (IMEM), Parma, is thanked for his interest in this study.

Supplementary data

Supplementary material related to this article can be found, in the online version, at https://doi.org/10.1016/j.jssc.2023.xxxxxx.

References

[1] H. Tian, J. He, X. Zhang, L. Zhou, D. Wang. Facile synthesis of porous manganese oxide K-OMS-2 materials and their catalytic activity for formaldehyde oxidation. Microp. Mesoporous Mater. 138 (2011) 118–122. doi.org/10.1016/j.micromeso.2010.09.022

[2] W. Ruettinger, L. Alden, P. Tran, D. Weinberger, A. Shi, F. Zhao. Catalyst device for treatment of formaldehyde and volatile organic compounds. Patent PCT/US2016/063040, 48p. https://patents.google.com/patent/WO2017105785A1/ko

[3] S. Rong, P. Zhang, F. Liu, Y. Yang. Engineering crystal facet of α-MnO_2 nanowire for highly efficient catalytic oxidation of carcinogenic airborne formaldehyde. ACS Catalysis 8 (2018) 3435–3446. doi.org/10.1021/acscatal.8b00456

[4] J. Hou, L. Liu, Y. Li, M. Mao, H. Lv, X. Zhao. Tuning the K^+ concentration in the tunnel of OMS-2 nanorods leads to a significant enhancement of the catalytic activity for benzene oxidation. Environ. Sci. Technol. 47 (2013) 13730−13736. doi.org/10.1021/es403910s

[5] B. Chen, B. Wu, L. Yu, M. Crocker, C. Shi. Investigation into the catalytic roles of various oxygen species over different crystal phases of MnO_2 for C_6H_6 and HCHO oxidation. ACS Catal. 10 (2020) 6176−6187. doi.org/10.1021/acscatal.0c00459

[6] Y.-C. Son, V.D. Makwana, A.R. Howell, S.L. Suib. Efficient, catalytic, aerobic oxidation

of alcohols with octahedral molecular sieves. Angew. Chem. Int. Ed. 40 (2001) 4280–4283. doi.org/10.1002/1521-3773(20011119)40:22<4280::AID-ANIE4280>3.0.CO;2-L

[7] Y.-S. Ding, X.-F. Shen, S. Sithambaram, S. Gomez, R. Kumar, V.M.B. Crisostomo, S.L. Suib, M. Aindow. Synthesis and catalytic activity of cryptomelane-type manganese dioxide nanomaterials produced by a novel solvent-free method. Chem. Mater. 17 (2005) 5382–5389. doi.org/10.1021/cm051294w

[8] F. Schurz, J.M. Bauchert, T. Merker, T. Schleid, H. Hasse, R. Gläser. Octahedral molecular sieves of the type K-OMS-2 with different particle sizes and morphologies: Impact on the catalytic properties in the aerobic partial oxidation of benzyl alcohol. Applied Catalysis A: General 355 (2009) 42–49. doi.org/10.1016/j.apcata.2008.11.014

[9] N.N. Opembe, C.K. King'ondu, A.E. Espinal, C.-H. Chen, E.K. Nyutu, V.M. Crisostomo, S.L. Suib. Microwave-assisted synthesis of manganese oxide octahedral molecular sieve (OMS-2) nanomaterials under continuous flow conditions. J. Phys. Chem. C 114 (2010) 14417–14426. doi.org/10.1021/jp104699p

[10] L. Espinal, W. Wong-Ng, J.A. Kaduk, A.J. Allen, C.R. Snyder, C. Chiu, D.W. Siderius, L. Li, E. Cockayne, A.E. Espinal, S.L. Suib. Time-dependent CO_2 sorption hysteresis in a one-dimensional microporous octahedral molecular sieve. J Am Chem Soc.134 (2012) 7944−7951. doi.org/10.1021/ja3014133

[11] Y. Muraoka, H. Chiba, T. Atou, M. Kikuchi, K. Hiraga, Y. Syono, S. Sugiyama, S. Yamamoto, J.-C. Grenier. Preparation of α-MnO_2 with an open tunnel. J.Solid State Chem. 144 (1999) 136−142. doi.org/10.1006/jssc.1999.8133

[12] Y. Lin, X. Cui, L. Li. Low-potential amperometric determination of hydrogen peroxide with a carbon paste electrode modified with nanostructured cryptomelane-type manganese oxides. Electrochemistry Communications 7 (2005) 166–172. doi.org/10.1016/j.elecom.2004.12.005

[13] F. Sauvage, J.-M. Tarascon, E. Baudrin. Preparation and electrochemical properties of nano-sized cryptomelane particles for the formation of potentiometric potassium ion sensors. Microchim. Acta. 164 (2009) 363–369. doi.org/10.1007/s00604-008-0067-5

[14] A. Fort, T. Addabbo, V. Vignoli, F. Bertocci, M. Mugnaini, A. Atrei, M. Gregorkiewitz. Gas-sensing properties and modeling of silver doped potassium hollandite. Sens Actuators B. 194 (2014) 427–439. doi.org/10.1016/j.snb.2013.12.102

[15] S. Liu, A.R. Akbashev, X. Yang, X. Liu, W. Li, L. Zhao, X. Li, A. Couzis, M.-G. Han, Y. Zhu, L. Krusin-Elbaum, J. Li, L. Huang, S.J.L. Billinge, J.E. Spanier, S. O'Brien. Hollandites as a new class of multiferroics. Scientific Reports 4 (2014) 6203, 6p. doi.org/10.1038/srep06203

[16] T. Ohzuku, M. Kitagawa, K. Sawai, T. Hiroi. Topotactic reduction of alpha-manganese (di)oxide in nonaqueous lithium cells. J. Electrochem. Soc. 138 (1991) 360–365. doi.org/10.1149/1.2085589

[17] M.H. Rossouw, D.C. Liles, M.M. Thackeray. Alpha manganese dioxide for lithium batteries: A structural and electrochemical study. Mat. Res. Bull. 27 (1992) 221–230. doi.org/10.1016/0025-5408(92)90216-M

[18] P. Botkovitz, P. Deniard, M. Tournoux, R. Brec. Structural and electrochemical characteristics of a hollandite-type 'Li_xMnO_2'. J. Power Sources, 43–44 (1993) 657–665. doi.org/10.1016/0378-7753(93)80216-C

[19] C.S. Johnson, D.W. Dees, M.F. Mansuetto, M.M. Thackeray, D.R. Vissers, D. Argyriou, C.-K. Loong, L. Christensen. Structural and electrochemical studies of α-manganese dioxide (α-MnO_2). J. Power Sources 68 (1997) 570–577. doi.org/10.1016/S0378-7753(96)02633-X

[20] N. Kijima, Y. Takahashi, J. Akimoto, J.Awaka. Lithium ion insertion and extraction reactions with Hollandite-type manganese dioxide free from any stabilizing cations in its tunnel cavity. J Solid State Chemistry 178 (2005) 2741–2750.

doi.org/10.1016/j.jssc.2005.06.023

[21] Z. Yang, L. Trahey, Y. Ren, M.K. Y. Chan, C. Lin, J. Okasinski, M.M. Thackeray. In situ high-energy synchrotron X-ray diffraction studies and first principles modeling of α-MnO_2 electrodes in Li–O_2 and Li-ion coin cells. J. Mater. Chem. A 3 (2015) 7389–7398. doi.org/10.1039/c4ta06633b

[22] M. Toupin, T. Brousse, D. Bélanger. Influence of microstucture on the charge storage properties of chemically synthesized manganese dioxide. Chem. Mater. 14 (2002) 3946–3952. doi.org/10.1021/cm020408q

[23] G. Wang, L.Zhang, J. Zhang. A review of electrode materials for electrochemical supercapacitors. Chem. Soc. Rev. 41 (2012) 797–828. doi.org/10.1039/C1CS15060J

[24] M. Huang, F. Li, F. Dong, Y.X. Zhang, L.L. Zhang. MnO_2-based nanostructures for high-performance supercapacitors. J. Mater. Chem. A 3 (2015) 21380–21423. doi.org/10.1039/c5ta05523g

[25] B.W. Byles, D.A. Cullen, K.L. More, E. Pomerantseva. Tunnel structured manganese oxide nanowires as redox active electrodes for hybrid capacitive deionization. Nano Energy. 44 (2018) 476–488. doi.org/10.1016/j.nanoen.2017.12.015

[26] Z.Y. Leong, H.Y. Yang. A study of MnO_2 with different crystalline forms for pseudocapacitive desalination. ACS Appl. Mater. Interfaces 11 (2019) 13176−13184. doi.org/10.1021/acsami.8b20880

[27] J. Fortunato, J. Peña, S. Benkaddour, H. Zhang, J. Huang, M. Zhu, B.E. Logan, C.A. Gorski. Surveying manganese oxides as electrode materials for harnessing salinity gradient energy. Environ. Sci .Technol. 54 (2020) 5746−5754. doi.org/10.1021/acs.est.0c00096

[28] D. Kohl. Surface processes in the detection of reducing gases with SnO_2-based devices. Sens. Actuators 18 (1989) 71–113. doi.org/10.1016/0250-6874(89)87026-X

[29] N. Yamazoe. New approaches for improving semiconductor gas sensors. Sens. Actuators

B 5 (1991) 7–19. doi.org/10.1016/0925-4005(91)80213-4

[30] N. Barsan, U. Weimar. Conduction model of metal oxide gas sensors. J. Electroceram. 7 (2001) 143–167. doi.org/10.1023/A:1014405811371

[31] R. Kumar, S. Sithambaram, S.L. Suib. Cyclohexane oxidation catalyzed by manganese oxide octahedral molecular sieves—Effect of acidity of the catalyst. J. Catalysis 262 (2009) 304–313. doi.org/10.1016/j.jcat.2009.01.007

[32] I. Djerdj, D. Sheptyakov, F. Gozzo, D. Arčon, R. Nesper, M. Niederberger. Oxygen self-doping in hollandite-type vanadium oxyhydroxide nanorods. J. Am. Chem. Soc. 130 (2008) 11364–11375. doi.org/10.1021/ja801813a

[33] A.S. Poyraz, J. Huang, C.J. Pelliccione, X. Tong, S. Cheng, L. Wu, Y. Zhu, A.C. Marschilok, K.J. Takeuchi, E.S. Takeuchi. Synthesis of cryptomelane type α-MnO_2 ($K_xMn_8O_{16}$) cathode materials with tunable K^+ content: the role of tunnel cation concentration on electrochemistry. J. Mater. Chem. A 5 (2017) 16914–16928. doi.org/10.1039/C7TA03476H

[34] Y. Zhang, J. Li, L. Peng, M. Ma, D. Gao, J. Bi, J. Wu. Formaldehyde sensing with a parts-per-billion limit of detection by dielectric properties and crystal symmetry optimization in $BiFeO_3$ -based p-type solid solution. Sens. Actuators B 344 (2021) 130314, 10p. doi.org/10.1016/j.snb.2021.130314

[35] T. Kohler, T. Armbruster, F. Libowitzky. Hydrogen bonding and Jahn–Teller distortion in groutite, α-MnOOH, and manganite, γ-MnOOH, and their relations to the manganese dioxides ramsdellite and pyrolusite. J. Solid State Chem. 133 (1997) 486–500. doi.org/10.1006/jssc.1997.7516

[36] R.W. Cheary, A. Coelho. A fundamental parameters approach to X-ray line-profile fitting. J. Appl. Crystallogr. 125 (1992) 109–121. doi.org/10.1107/S0021889891010804

[37] L.W. Finger, D.E. Cox, A.P. Jephcoat. A correction for powder diffraction peak

asymmetry due to axial divergence. J. Appl. Crystallogr. 27 (1994) 892–900. doi.org/10.1107/S0021889894004218

[38] P.W. Stephens. Phenomenological model of anisotropic peak broadening in powder diffraction. J. Appl. Crystallogr. 32 (1999) 281–289. doi.org/10.1107/S0021889898006001

[39] D. Balzar, N. Audebrand, M.R. Daymond, A. Fitch, A. Hewat, J.I. Langford, A. Le Bail, D. Louër, O. Masson, C.N. McCowan, N.C. Popa, P.W. Stephens, B.H. Toby. Size–strain line-broadening analysis of the ceria round-robin sample. J. Appl. Crystallogr. 37 (2004) 911–924. doi.org/10.1107/S0021889804022551

[40] L. Lutterotti, H. Pillière, C. Fontugne, P. Boullay, D. Chateigner. Full-profile search–match by the Rietveld method. J. Appl. Crystallogr. 52 (2019) 587–598. doi.org/10.1107/S160057671900342X

[41] M. Pasero. A short outline of the tunnel oxides. Rev. Mineral. Geochem. 57 (2005) 291–305. doi.org/10.2138/rmg.2005.57.9

[42] K. Momma, F. Izumi. VESTA 3 for three-dimensional visualization of crystal, volumetric and morphology data. J. Appl. Crystallogr. 44 (2011) 1272–1276. doi.org/10.1107/S0021889811038970

[43] R.N. DeGuzman, Y.-F. Shen, E.J. Neth, S.L. Suib, C.-L. O'Young, S. Levine, J.M. Newsam. Synthesis and characterization of octahedral molecular sieves (OMS-2) having the hollandite structure. Chem. Mater. 6 (1994) 815–821. doi.org/10.1021/cm00042a019

[44] A.C. Larson, R.B. Von Dreele. *General Structure Analysis System (GSAS)*. Los Alamos National Laboratory Report LAUR 86-748 (2004). https://subversion.xray.aps.anl.gov/trac/EXPGUI/wiki/InstallLinux

[45] B.H. Toby. EXPGUI, a graphical user interface for GSAS. J. Appl. Crystallogr. 34 (2001) 210–213. doi.org/10.1107/S0021889801002242

[46] P. Thompson, D.E. Cox, J.B. Hastings. Rietveld refinement of Debye-Scherrer

synchrotron X-ray data from Al_2O_3. J. Appl. Crystallogr. 20 (1987) 79–83. doi.org/10.1107/S0021889887087090

[47] G. Caglioti, A. Paoletti, F.P. Ricci. Choice of collimators for a crystal spectrometer for neutron diffraction. Nucl. Instrum. 3 (1958) 223–228. doi.org/10.1016/0369-643X(58)90029-X

[48] Scilab Enterprises. *Scilab: free and open source software for numerical computation*. Scilab Enterprises, Orsay, France, www.scilab.org (2012).

[49] J. Vicat, E. Fanchon, P. Strobel, D.T. Qui. The structure of $K_{1.33}Mn_8O_{16}$ and cation ordering in hollandite-type structures. Acta Crystallogr. B 42 (1986) 162–167. doi.org/10.1107/S0108768186098415

[50] L. Lutterotti. Total pattern fitting for the combined size-strain-stress-texture determination in thin film diffraction. Nucl. Instrum. Methods Phys. Res. B 268 (2010) 334–340. doi.org/10.1016/j.nimb.2009.09.053

[51] J.E. Post, R.B. Von Dreele, P.R. Buseck. Symmetry and cation displacements in hollandites: structure refinements of hollandite, cryptomelane and priderite. Acta Crystallogr. B 38 (1982) 1056–1065. doi.org/10.1107/S0567740882004968

[52] J.E. Post, C.W. Burnham. Modeling tunnel-cation displacements in hollandites using structure-energy calculations. Am. Mineral. 71 (1986) 1178–1185. www.minsocam.org/ammin/AM71/AM71_1178.pdf

[53] Y. Michiue. Probability density analyses of guest ions in hollandite $A_xMg_{x/2}Ti_{8-x/2}O_{16}$ (A = K, Rb). Acta Crystallogr. B 63 (2007) 577–583. doi.org/10.1107/S0108768107023531

[54] W.H. Hall. X-ray line broadening in metals. Proc. Phys. Soc. London Sect. A 62 (1949) 741–743. doi.org/10.1088/0370-1298/62/11/110

[55] G.K. Williamson, W.H. Hall. X-ray line broadening from filed aluminium and wolfram. Acta Metall. 1 (1953) 22–31. doi.org/10.1016/0001-6160(53)90006-6

[56] R.M. McKenzie. The synthesis of birnessite, cryptomelane, and some other oxides and hydroxides of manganese. Mineral. Mag. 38 (1971) 493–502. doi.org/10.1180/minmag.1971.038.296.12

[57] D. Portehault, S. Cassaignon, E. Baudrin, J.-P. Jolivet. Morphology control of cryptomelane type MnO_2 nanowires by soft chemistry, Growth mechanisms in aqueous medium. Chem. Mater. 19 (2007) 5410–5417. doi.org/10.1021/cm071654a

[58] S. Ching, D.A. Kriz, K.M. Luthy, E.C. Njagi, S.L. Suib. Self-assembly of manganese oxide nanoparticles and hollow spheres. Catalytic activity in carbon monoxide oxidation. Chem. Commun. 47 (2011) 8286–8288. doi.org/10.1039/c1cc11764e

[59] N. Birkner, A. Navrotsky. Thermodynamics of manganese oxides: sodium, potassium, and calcium birnessite and cryptomelane. Proc. Natl. Acad. Sci. U.S.A. 114 (2017) E1046–E1053. doi.org/10.1073/pnas.1620427114

[60] K. Maniammal, G. Madhu, V. Biju. X-ray diffraction line profile analysis of nanostructured nickel oxide: shape factor and convolution of crystallite size and microstrain contributions. Physica E 85 (2017) 214–222. doi.org/10.1016/j.physe.2016.08.035

[61] A. Leineweber. Reflection splitting-induced microstrain broadening. Powder Diffr. 32 (2017) 35–39. doi.org/10.1017/S0885715617000665

[62] J. Rodríguez-Carvajal, M.T. Fernández-Díaz, J.L. Martínez. Neutron diffraction study on structural and magnetic properties of La_2NiO_4. J. Phys. Condens. Matter. 3 (1991) 3215–3234. doi.org/10.1088/0953-8984/3/19/002

[63] J. Rodríguez-Carvajal. *Structural analysis from powder diffraction data: the Rietveld method.* École Thématique: Cristallographie et Neutrons, Batz-sur-Mer, 12-13 may 1997, 25 p.

[64] P. Fabrykiewicz, R. Przeniosło, I. Sosnowska, F. Fauth, D. Oleszak. Verification of the de Wolff hypothesis concerning the symmetry of β-MnO_2. Acta Crystallogr. A 75 (2019) 889–

901. doi.org/10.1107/S2053273319013408

[65] T. Gao, M. Glerup, F. Krumeich, R. Nesper, H. Fjellvåg, P. Norby. Microstructures and spectroscopic properties of cryptomelane-type manganese dioxide nanofibers. J. Phys. Chem. C 112 (2008) 13134–13140. doi.org/10.1021/jp804924f

[66] L. Ma, T. Hartmann, M.A. Cheney, N.R. Birkner, P.K. Bhowmik. Characterization of an inorganic cryptomelane nanomaterial synthesized by a novel process using transmission electron microscopy and X-ray diffraction. Microsc. Microanal. 14 (2008) 328–334. doi.org/10.1017/S1431927608080367